



# Spatial and electronic effects synergistically enhanced electrocatalytic oxygen evolution using atomic iridium-anchored cobalt oxyhydroxide nanosheets

Bo Yang <sup>a</sup>, Meiqian Li <sup>a</sup>, Zhirong Zhang <sup>b</sup>, Shaoqing Chen <sup>c</sup>, Miaoqiao Wang <sup>d</sup>, Li Sheng <sup>b</sup>, Libo Deng <sup>a</sup>, Rui Si <sup>e</sup>, Maohong Fan <sup>f</sup>, Huihuang Chen <sup>a,\*</sup>

<sup>a</sup> College of Chemistry and Environmental Engineering, Shenzhen University, Shenzhen 518060, PR China

<sup>b</sup> Hefei National Laboratory for Physical Sciences at the Microscale, University of Science and Technology of China, Hefei 230026, PR China

<sup>c</sup> Innovation Center for Chemical Sciences, College of Chemistry, Chemical Engineering and Materials Science, Soochow University, Suzhou 215123, PR China

<sup>d</sup> Institute of Advanced Science Facilities, Shenzhen (IASF), Shenzhen 518060, PR China

<sup>e</sup> Shanghai Synchrotron Radiation Facility, Shanghai Institute of Applied Physics, Chinese Academy of Sciences, Shanghai 201204, PR China

<sup>f</sup> Departments of Chemical and Petroleum Engineering, University of Wyoming, WY 82071, USA



## ARTICLE INFO

### Keywords:

Dangling single-atom catalysts  
Unsaturated coordination  
Spatial regulation catalysis  
Synergistic effect  
Rechargeable zinc-air battery

## ABSTRACT

Single-atom catalysts (SACs) based on noble metals play irreplaceable roles in the field of catalysis but unfortunately suffer from spatial constraints ranging from either lattice substitution, atomic dilution, or in-layer immobilization. Herein, this work was designed to overcome the limitation by locating discrete dangling coordinatively unsaturated  $[IrO_5]$  motif atop  $\gamma$ -phase cobalt oxyhydroxide ( $\gamma$ -CoOOH) nanosheets to create a spatially novel catalyst ( $Ir_1/CoOOH_{sur}$ ). For comparison, the lattice-doped catalyst ( $Ir_1/CoOOH_{lat}$ ) was also synthesized via substituting Co in  $\gamma$ -CoOOH by Ir single atoms. The distinct location arrangements of Ir single atoms generated two different active sites that both weakened the adsorption of oxygenated intermediates relative to  $\gamma$ -CoOOH due to the upshifted O 2p-band center. Moreover,  $Ir_1/CoOOH_{sur}$  displayed a much weaker adsorption capability (closer to an ideal catalyst) than  $Ir_1/CoOOH_{lat}$ . Therefore, the spatial and electronic effects of discrete dangling  $[IrO_5]$  motifs atop  $Ir_1/CoOOH_{sur}$  synergistically optimized the adsorption of oxygenated intermediates and thus gained the lowest energy barrier of the rate-determining step for oxygen evolution reaction. When used as the cathode catalyst in rechargeable zinc-air batteries,  $Ir_1/CoOOH_{sur}$  exhibited higher power density (101 mW  $cm^{-2}$ ) and cycling durability (800 h) than  $IrO_2$  (94 mW  $cm^{-2}$ , 50 h). This study broadens noble metal-based SACs analogues and offers appealing opportunity to design target catalysts with the synergism of spatial and electronic effects for diverse catalytic applications.

## 1. Introduction

Oxygen evolution reaction (OER) powered by renewable electricity is crucial for diverse sustainable (photo)electrochemical energy storage and conversion technologies, such as water splitting, carbon dioxide reduction, and rechargeable zinc-air batteries [1–5]. Unfortunately, the sluggish kinetics of OER at the anode requires a substantially higher energy barrier than the corresponding reductive half-reaction at the cathode, which significantly restricts the overall efficiency [6–8]. The OER benchmark electrocatalysts  $IrO_2$  and  $RuO_2$  suffer from scarcity and high cost, which limit the large-scale application [9]. As such, the development of earth-abundant, high-performance, and durable

electrocatalysts have received huge attention in the past decades.

Recently, regulating the spatial configuration and electronic structure of active sites in single-atom catalysts (SACs) has been proven successful in tuning the binding of reactants and intermediates that governs the catalytic performance [10–16]. In such context, various SACs have been designed and synthesized to enhance the catalytic activity and stability in electro-, photo- and thermo-catalysis fields [17–24]. For instance, by varying the location of discrete  $[IrO_6]$  octahedra, the adsorption strength of oxygenated intermediates could be efficiently tuned to reduce the energy barrier toward OER [25]. The precisely engineered electronic structure of Ru single atoms in PtCu alloys via compressive strain also boosted the kinetically sluggish OER

\* Corresponding author.

E-mail address: [hhchen@ustc.edu.cn](mailto:hhchen@ustc.edu.cn) (H. Chen).

[26]. However, prior endeavors primarily focused on SACs that are either encapsulated in the bulk lattice through cation substitution [27–29], diluted in single-atom alloys [30–35], or fixed in graphene-like 2D layers coordinated with C/N/O/S/P atoms [36–41], which generally failed to fully expose the active site. Dangling coordinatively unsaturated SACs anchored atop heterogenous catalysts should be more prone to maximizing the accessibility of active sites and tuning adsorption energy of oxygenated intermediates to enable intrinsically higher OER performance [42], and yet have been barely reported in the literature.

Herein, this study takes a critical step to fulfill the aforesaid research gap by synthesizing two Ir-based SACs with distinct spatial configuration and electronic structure.  $\gamma$ -CoOOH was used as a support to avoid structural reconstruction under oxidative conditions and better elucidate the structure-function relationship. Discrete dangling coordinatively unsaturated  $[IrO_5]$  motifs were anchored atop  $\gamma$ -CoOOH ( $Ir_1/CoOOH_{sur}$ ) through in-situ cryogenic-photochemical strategy. In contrast, substituting Co in  $\gamma$ -CoOOH by Ir single atoms yielded the lattice-doped catalyst ( $Ir_1/CoOOH_{lat}$ ). The upshifted O 2p-band center of  $Ir_1/CoOOH_{sur}$  and  $Ir_1/CoOOH_{lat}$  relative to that of  $\gamma$ -CoOOH weakened the adsorption of oxygenated intermediates and dramatically enhanced their electrocatalytic OER performance. Of note, the free-energy diagram for OER over  $Ir_1/CoOOH_{sur}$  was closer to that over an ideal catalyst, thus warranting  $Ir_1/CoOOH_{sur}$  the minimum energy barrier toward OER. The specific activity of  $Ir_1/CoOOH_{sur}$  was approximately 5 and 11 times higher than that of  $Ir_1/CoOOH_{lat}$  and  $IrO_2$ , respectively. When applied in rechargeable zinc-air batteries,  $Ir_1/CoOOH_{sur}$  owned higher power density ( $101\text{ mW cm}^{-2}$ ) and cycling durability (800 h) than  $IrO_2$  ( $94\text{ mW cm}^{-2}$ , 50 h). This work is novel in terms of synthesis method, active site and steric configuration, which broadens SACs analogues and efficaciously modulates the spatial configuration and electronic structure that synergistically improve the catalytic performance.

## 2. Materials and methods

### 2.1. Synthesis of $\alpha$ -Co(OH)<sub>2</sub>

$\alpha$ -Co(OH)<sub>2</sub> was synthesized in a beaker under ambient conditions based on a previous report with some modifications [43]. Typically, anhydrous cobalt chloride (CoCl<sub>2</sub>, 6 mM), sodium chloride (NaCl, 30 mM) and hexamethylenetetramine (HMT, C<sub>6</sub>H<sub>12</sub>N<sub>4</sub>, 36 mM) were dissolved in a mixture of deionized water (600 mL) and ethanol (60 mL) to obtain a pink-colored solution. The resultant solution was then heated at 90 °C under continuous stirring for 2 h to yield green-particle containing suspension, which was centrifuged and thoroughly washed with deionized water and anhydrous ethanol. The solid product was finally dried in a vacuum oven at 40 °C for further use.

### 2.2. Synthesis of $\gamma$ -CoOOH

$\gamma$ -CoOOH was synthesized via oxidizing  $\alpha$ -Co(OH)<sub>2</sub> using sodium hypochlorite (NaClO). Specifically,  $\alpha$ -Co(OH)<sub>2</sub> was added into a mixture of deionized water and anhydrous ethanol followed by vigorous stirring to form a uniform solution. The pH value of the obtained solution was adjusted to 12 using 0.5 M NaOH. Subsequently, NaClO (available chlorine 5.5%–6.5%, 21 mL) was added dropwise under vigorous stirring and kept stirring for 1 h prior to setting for 0.5 h. The brown black suspension was then centrifuged and thoroughly washed with deionized water. The solid product was finally dried in a vacuum oven at 40 °C for further use.

### 2.3. Synthesis of $Ir_1/CoOOH_{sur}$

$Ir_1/CoOOH_{sur}$  was synthesized via in-situ cryogenic-photochemical strategy referring a previous report [44]. Firstly,  $\gamma$ -CoOOH (1 mg) was added into 10 mL IrCl<sub>3</sub> (2.33 mg L<sup>-1</sup>) containing aqueous solution under ultrasound to obtain a homogeneous dispersion system in a petri dish.

The petri dish was frozen quickly in a liquid nitrogen bath to ensure the uniform dispersion of Ir precursor. Secondly, UV irradiation was performed on the frozen sample for 1 h in an environment chamber (−40 °C), in order to prevent ice melting and obtain Ir single atoms on  $\gamma$ -CoOOH support. Whereafter, the sample was defrosted, centrifuged and washed with deionized water, and then freeze-dried.

### 2.4. Synthesis of $Ir_1/CoOOH_{lat}$

$Ir_1/CoOOH_{lat}$  was synthesized using similar procedures. Firstly, Ir doped Co(OH)<sub>2</sub> was synthesized by dissolving anhydrous cobalt chloride (CoCl<sub>2</sub>, 6 mM), sodium chloride (NaCl, 30 mM), iridium chloride (IrCl<sub>3</sub>, 0.0435 mM) and hexamethylenetetramine (C<sub>6</sub>H<sub>12</sub>N<sub>4</sub>, 36 mM) in a mixture of deionized water (600 mL) and ethanol (60 mL). The resultant solution was then heated at 90 °C under continuous stirring for 2 h, which was centrifuged and thoroughly washed with deionized water and anhydrous ethanol. The solid product was dried in a vacuum oven at 40 °C to obtain Ir doped Co(OH)<sub>2</sub>. Secondly, Ir doped Co(OH)<sub>2</sub> was oxidized by NaClO to form Ir doped CoOOH ( $Ir_1/CoOOH_{lat}$ ) using the aforementioned method.

### 2.5. Electrochemical measurements

A CHI760E electrochemical station was used to evaluate the electrocatalytic performance under ambient conditions. The work electrode, counter electrode and reference electrode was catalyst-coated glassy carbon electrode (d=3 mm), graphite rod and Hg/HgO, respectively. A homogeneous catalyst ink was obtained by thoroughly mixing carbon black (2 mg), catalyst (2 mg), Nafion (50  $\mu$ L), deionized water (0.5 mL) and ethanol (0.45 mL) under sonication for 1 h. To prepare the work electrode, 5  $\mu$ L catalyst ink was then dropped onto the surface of glassy carbon electrode to form a uniform film. The temperature of catholyte and anolyte was constant (25 °C) during the reaction. LSV curves were collected in an O<sub>2</sub> pre-saturated 1.0 M KOH aqueous electrolyte with a scanning rate of 5 mV s<sup>-1</sup>. The potentials in this work were converted to reversible hydrogen electrode (RHE) using the equation  $E_{RHE} = E_{Hg/HgO} + 0.0591 V \times pH + 0.098 V$ . All potentials were acquired without  $iR$  corrections ( $i$ , current;  $R$ , resistance). The weight percent of Ir in  $Ir_1/CoOOH_{sur}$  and  $Ir_1/CoOOH_{lat}$  was 0.7 wt% and 1.9 wt%, respectively. Electrochemical impedance spectroscopy (EIS) was recorded at the potential of 1.53 V vs. RHE with the frequency ranging from 100 kHz to 0.01 Hz. TOF values were calculated based on the activity of the catalysts per active site using the equation  $TOF = (j \times A) / (4 \times F \times m)$ , in which  $j$  is the current density at a given overpotential,  $A$  is the geometric surface area of the electrode,  $F$  is the Faraday constant, and  $m$  is the moles of Ir atoms. The amount of O<sub>2</sub> produced during OER was determined using a gas chromatography equipped with Molecular sieve 5 A capillary column and a thermal conductivity detector. Experimental data was collected at a current density of 10 mA cm<sup>-2</sup> for 150 min. The theoretical Faradic efficiency (FE) of O<sub>2</sub> was calculated using the equation  $FE = 4 F \times nO_2 / Q$ , where  $F$  is the Faraday constant,  $nO_2$  is the total amount of O<sub>2</sub> produced, and  $Q$  is the total charge passed through the electrolytic cell. The electrochemical active surface area (ECSA) of the electrode was estimated using the equation  $ECSA = R_f \times S$ , where  $R_f$  is the roughness factor and  $S$  is the geometric area of working electrodes. Double layer capacitance (C<sub>dl</sub>) was determined using cyclic voltammetry at varied scan rates.  $R_f$  was calculated via  $R_f = C_{dl}/60 \mu\text{F cm}^{-2}$  ( $C_{dl}$  for an ideal smooth oxide surface is 60  $\mu\text{F cm}^{-2}$ ).

### 2.6. Rechargeable zinc-air battery test

To further verify the catalytic performance of  $Ir_1/CoOOH_{sur}$ , it was applied to a rechargeable zinc-air battery. The rechargeable Zn-air battery was assembled using a zinc plate as anode (thickness: 0.1 mm),  $Ir_1/CoOOH_{sur}$ -loaded carbon paper (catalyst loading: 1 mg cm<sup>-2</sup>) as the air electrode with the separator of Celgard 3560. The electrolyte

was a mixture of 6.0 M KOH and 0.2 M zinc acetate solution. For comparison, a Zinc-air battery using the benchmark commercial  $\text{IrO}_2$  catalyst was also assembled and tested. All the battery test was conducted using a LAND CT2001A battery testing system.

### 2.7. Materials characterizations and computational methods

Details for materials characterizations and the computational details are provided in the [Supporting Information](#).

## 3. Results and discussion

### 3.1. Synthesis and characterizations

Ir-based SACs ( $\text{Ir}_1/\text{CoOOH}_{\text{sur}}$  and  $\text{Ir}_1/\text{CoOOH}_{\text{lat}}$ ) were synthesized via a hydrothermal method and in-situ cryogenic-photochemical strategy as illustrated in Schematic 1.  $\text{Ir}_1/\text{CoOOH}_{\text{lat}}$  was obtained by oxidizing Ir single atoms-doped  $\alpha\text{-Co(OH)}_2$  ( $\text{Ir}_1/\text{Co(OH)}_2$ ) using the

oxidant  $\text{NaClO}$ .  $\text{Ir}_1/\text{CoOOH}_{\text{sur}}$  was acquired by means of in-situ cryogenic-photochemical synthesis to ensure that the discrete dangling  $[\text{IrO}_x]$  motif was anchored atop  $\gamma\text{-CoOOH}$  nanosheets. Transmission electron microscopy (TEM) image of  $\alpha\text{-Co(OH)}_2$  nanosheets shows a smooth hexagonal platelet-shaped morphology (Fig. S1a), which underwent fracture after being oxidized to  $\gamma\text{-CoOOH}$  nanosheets (Fig. S1b). The morphology of polycrystalline  $\text{Ir}_1/\text{CoOOH}_{\text{sur}}$  and  $\text{Ir}_1/\text{CoOOH}_{\text{lat}}$  resembles that of  $\gamma\text{-CoOOH}$  nanosheets, although the surface of  $\text{Ir}_1/\text{CoOOH}_{\text{lat}}$  was a bit rougher (Fig. S1d-i). Atomic force microscopy (AFM) images exhibit that the thickness of  $\gamma\text{-CoOOH}$  and  $\text{Ir}_1/\text{CoOOH}_{\text{sur}}$  is ca. 6 nm and that of  $\text{Ir}_1/\text{CoOOH}_{\text{lat}}$  is ca. 8 nm (Fig. S2), indicating that in-situ doping Ir into the lattice during the hydrothermal process promoted the vertical growth of  $\alpha\text{-Co(OH)}_2$  nanosheets. This discrepancy can also be confirmed by the enhanced  $\text{N}_2$  adsorption-desorption isotherms and larger Brunauer-Emmett-Teller (BET) surface area of  $\text{Ir}_1/\text{CoOOH}_{\text{lat}}$  (Fig. S3; Table S1).

Double Cs-corrected scanning transmission electron microscopy (STEM) in high-angle annular dark field (HAADF) mode was employed

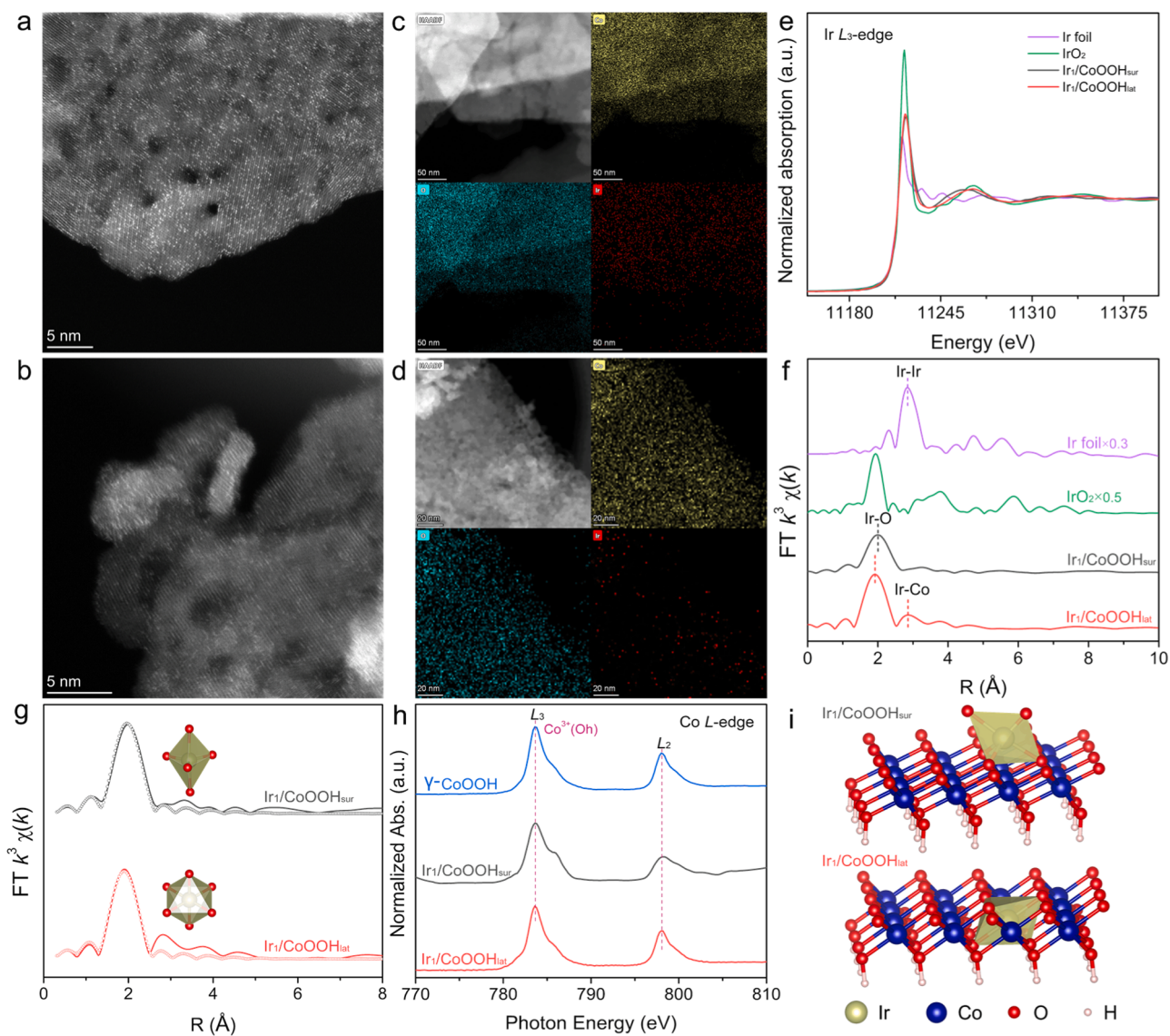


**Fig. 1.** Electronic and chemical structure of  $\text{Ir}_1/\text{CoOOH}_{\text{sur}}$  and  $\text{Ir}_1/\text{CoOOH}_{\text{lat}}$ . Double Cs-corrected HAADF-STEM images of (a)  $\text{Ir}_1/\text{CoOOH}_{\text{sur}}$  and (b)  $\text{Ir}_1/\text{CoOOH}_{\text{lat}}$ . Atomic-resolution EDX elemental mappings of (c)  $\text{Ir}_1/\text{CoOOH}_{\text{sur}}$  and (d)  $\text{Ir}_1/\text{CoOOH}_{\text{lat}}$ . Normalized (e) XANES and (f)  $\text{Ir L}_3$ -edge EXAFS spectra of  $\text{Ir}_1/\text{CoOOH}_{\text{sur}}$  and  $\text{Ir}_1/\text{CoOOH}_{\text{lat}}$ . Ir foil and  $\text{IrO}_2$  were used as the references. (g) Experimental and fitted  $\text{Ir L}_3$ -edge EXAFS spectra of  $\text{Ir}_1/\text{CoOOH}_{\text{sur}}$  and  $\text{Ir}_1/\text{CoOOH}_{\text{lat}}$ . The insets show the first-shell Ir-O coordination geometry of  $\text{Ir}_1/\text{CoOOH}_{\text{sur}}$  and  $\text{Ir}_1/\text{CoOOH}_{\text{lat}}$ . (h) Co  $L$ -edge sXAS spectra of  $\gamma\text{-CoOOH}$ ,  $\text{Ir}_1/\text{CoOOH}_{\text{sur}}$  and  $\text{Ir}_1/\text{CoOOH}_{\text{lat}}$ .  $\text{Co}^{3+}(\text{OH})$  stands for  $\text{Co}^{3+}$  cation in the octahedral site. (i) Schematic representation of the crystalline structure model of  $\text{Ir}_1/\text{CoOOH}_{\text{sur}}$  and  $\text{Ir}_1/\text{CoOOH}_{\text{lat}}$ .

to validate the atomic dispersion of Ir for  $\text{Ir}_1/\text{CoOOH}_{\text{sur}}$  and  $\text{Ir}_1/\text{CoOOH}_{\text{lat}}$  by taking advantage of its heavier Z-contrast relative to the support (Fig. 1a,b). It is clear that Ir atoms (represented by bright spots) are atomically dispersed across the support, which is further demonstrated by the atomic-resolution energy-dispersive X-ray (EDX) elemental mappings (Fig. 1c,d). X-ray absorption near-edge spectroscopy (XANES) and extended X-ray absorption fine structure (EXAFS) of  $\text{Ir}_1/\text{CoOOH}_{\text{sur}}$  and  $\text{Ir}_1/\text{CoOOH}_{\text{lat}}$  were investigated to reveal the electronic structure and coordination environment of Ir single atoms. As can be seen in the Ir  $L_3$ -edge XANES spectra, the white line intensity of  $\text{Ir}_1/\text{CoOOH}_{\text{lat}}$  is close to that of  $\text{Ir}_1/\text{CoOOH}_{\text{sur}}$  and both straddle between Ir foil and  $\text{IrO}_2$ , indicating that the valence state of Ir in the lattice and atop the surface is higher than 0 and lower than 4 (Fig. 1e).

The detailed coordination environment of Ir single atoms can be unravelled by the Ir  $L_3$ -edge EXAFS spectra (Fig. 1f). The absence of Ir–Ir bond for  $\text{Ir}_1/\text{CoOOH}_{\text{sur}}$  and  $\text{Ir}_1/\text{CoOOH}_{\text{lat}}$  further proves the atomic dispersion of Ir. Both samples have a prominent peak at approximately 2.0 Å that is ascribed to the first-shell Ir–O scattering pathway as referred to  $\text{IrO}_2$ . It should be noted that the peak position (2.0 Å) of  $\text{Ir}_1/\text{CoOOH}_{\text{sur}}$  is larger than that (1.92 Å) of  $\text{Ir}_1/\text{CoOOH}_{\text{lat}}$ . This implies that  $\text{Ir}_1/\text{CoOOH}_{\text{sur}}$  has a longer Ir–O bond distance than  $\text{Ir}_1/\text{CoOOH}_{\text{lat}}$  owing to the loose bonding of the exposed discrete dangling  $[\text{IrO}_x]$  motif atop the support, in comparison to the compressively confined  $[\text{IrO}_6]$  octahedra in the lattice of  $\text{Ir}_1/\text{CoOOH}_{\text{lat}}$ . A weaker peak at 2.90 Å assigned to the second-shell Ir–Co (Ir–O–Co) scattering pathway was also observed in the EXAFS spectrum of  $\text{Ir}_1/\text{CoOOH}_{\text{lat}}$ , which is unobservable in the EXAFS spectrum of  $\text{Ir}_1/\text{CoOOH}_{\text{sur}}$ . These results coincide well with previous reports [25,27] and unambiguously corroborate that Ir single atoms substituted the lattice Co in  $\text{Ir}_1/\text{CoOOH}_{\text{lat}}$  whereas resided in the discrete dangling  $[\text{IrO}_x]$  motif atop  $\text{Ir}_1/\text{CoOOH}_{\text{sur}}$ . As the wavelet transform (WT)-EXAFS can discriminate the backscattering atoms in both k and R spaces with high resolution, we further analyzed the WT-EXAFS of  $\text{Ir}_1/\text{CoOOH}_{\text{sur}}$  (Fig. S4). Consistent with FT analysis,  $\text{Ir}_1/\text{CoOOH}_{\text{sur}}$  displayed only one characteristic region for Ir–O scattering with a local maximum at  $R = 1.6$  Å and  $k = 2.78$  Å<sup>-1</sup>, resembling that of  $\text{IrO}_2$ . This unambiguously verifies that the vast majority of Ir were in the form of single atoms. The absence of signal ( $R = 2.6$  Å and  $k = 10$  Å<sup>-1</sup>) excludes the contribution of Ir–Ir bond, further demonstrating the atomic dispersion of Ir atoms. It should be noted that the discrete dangling  $[\text{IrO}_x]$  motif should be more prone to exposing active sites, which is vital in the field of heterogeneous catalysis. The first-shell Ir–O coordination number (CN) is determined to be 5 and 6 for  $\text{Ir}_1/\text{CoOOH}_{\text{sur}}$  and  $\text{Ir}_1/\text{CoOOH}_{\text{lat}}$ , respectively, after fitting the experimental EXAFS data (Fig. 1g; Fig. S5; Table S2). The unsaturated coordination environment of Ir single atoms in  $\text{Ir}_1/\text{CoOOH}_{\text{sur}}$  not only contributed to the loose bonding of the exposed discrete dangling  $[\text{IrO}_5]$  motif as observed in Fig. 1f, but also provided a promising opportunity to tailor the intermediate adsorption capability. We determined the most energetically

favourable location for the discrete dangling  $[\text{IrO}_5]$  motif atop  $\text{Ir}_1/\text{CoOOH}_{\text{sur}}$  by considering possible slab models (Fig. S6). It is found that the face-centered cubic site was the most energetically stable model with the minimum formation energy via sharing three surface oxygen with the  $\gamma$ -CoOOH support (Table S3). The electronic structure of Co for  $\gamma$ -CoOOH,  $\text{Ir}_1/\text{CoOOH}_{\text{sur}}$  and  $\text{Ir}_1/\text{CoOOH}_{\text{lat}}$  was investigated using soft X-ray absorption spectroscopy (sXAS) (Fig. 1h). Negligible change occurred for the Co  $L$ -edge sXAS spectra of  $\gamma$ -CoOOH,  $\text{Ir}_1/\text{CoOOH}_{\text{sur}}$  and  $\text{Ir}_1/\text{CoOOH}_{\text{lat}}$ , suggesting an unaltered valence state and octahedral coordination configuration of Co for all samples. Based on the above characterizations, the structural model of  $\text{Ir}_1/\text{CoOOH}_{\text{sur}}$  and  $\text{Ir}_1/\text{CoOOH}_{\text{lat}}$  is schematically depicted in Fig. 1i.

The crystal structure of as-prepared samples was characterized by X-ray diffraction (XRD). The diffraction peaks of as-prepared  $\text{Co}(\text{OH})_2$  are in line with the (003), (006), (101), (012) and (015) planes of  $\alpha$ - $\text{Co}(\text{OH})_2$ , which coincides well with previous report (Fig. 2a) [43]. After being oxidized,  $\alpha$ - $\text{Co}(\text{OH})_2$  was transformed to  $\gamma$ -phase cobalt oxyhydroxide ( $\gamma$ -CoOOH) as evidenced by the (003) and (006) planes at 13.9 and 28.1°, respectively [45]. In addition, the full width at half maximum of the oxidized samples is larger than that of  $\alpha$ - $\text{Co}(\text{OH})_2$ , indicating the decreasing particle size based on the Scherrer equation. This coincides well with TEM images. X-ray photoelectron spectroscopy (XPS) was performed to further reveal the valence state of Co (Fig. 2b). The peaks of  $\gamma$ -CoOOH located at 794.7 and 779.7 eV are attributed to Co  $2p_{1/2}$  and Co  $2p_{3/2}$ , respectively, which verify the exclusive presence of  $\text{Co}^{3+}$  [46]. The almost identical Co  $2p$  XPS spectra of  $\gamma$ -CoOOH,  $\text{Ir}_1/\text{CoOOH}_{\text{sur}}$  and  $\text{Ir}_1/\text{CoOOH}_{\text{lat}}$  suggest that the valence state of Co remained the same after introducing Ir single atoms whether atop the surface or within the lattice, which agrees well with the Co  $L$ -edge sXAS spectra (Fig. 1h). The Ir  $4f$  and O  $1s$  XPS spectra are also observed in the samples (Fig. S7). Notably, the Raman peaks corresponding to  $\gamma$ -CoOOH are observed at 493 and 591 cm<sup>-1</sup> for all samples (Fig. 2c), further indicating the unchanged crystal structure [47]. These results collectively affirm that the presence of Ir single atoms with distinct coordination structures did not modify the crystal structure of the  $\gamma$ -CoOOH substrate.

### 3.2. Electrocatalytic OER performance

The electrocatalytic OER performance of  $\text{Ir}_1/\text{CoOOH}_{\text{sur}}$  and  $\text{Ir}_1/\text{CoOOH}_{\text{lat}}$  was assessed in comparison with as-fabricated  $\gamma$ -CoOOH and the benchmark catalyst  $\text{IrO}_2$ . As shown in the polarization curves (Fig. 3a), both  $\text{Ir}_1/\text{CoOOH}_{\text{sur}}$  (453 mV) and  $\text{Ir}_1/\text{CoOOH}_{\text{lat}}$  (461 mV) display an obviously lower overpotential at the current density of 10 mA cm<sup>-2</sup> compared with  $\gamma$ -CoOOH (510 mV), demonstrating that the enhanced electrocatalytic activity should be attributed to Ir single atoms. It is worth noting that  $\text{Ir}_1/\text{CoOOH}_{\text{sur}}$  exhibits the highest current density over the applied potential range, surpassing the benchmark

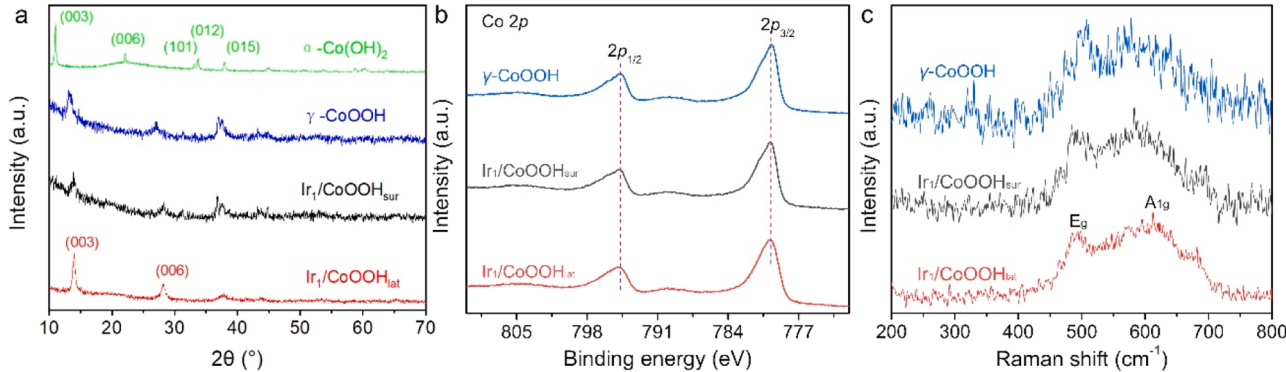
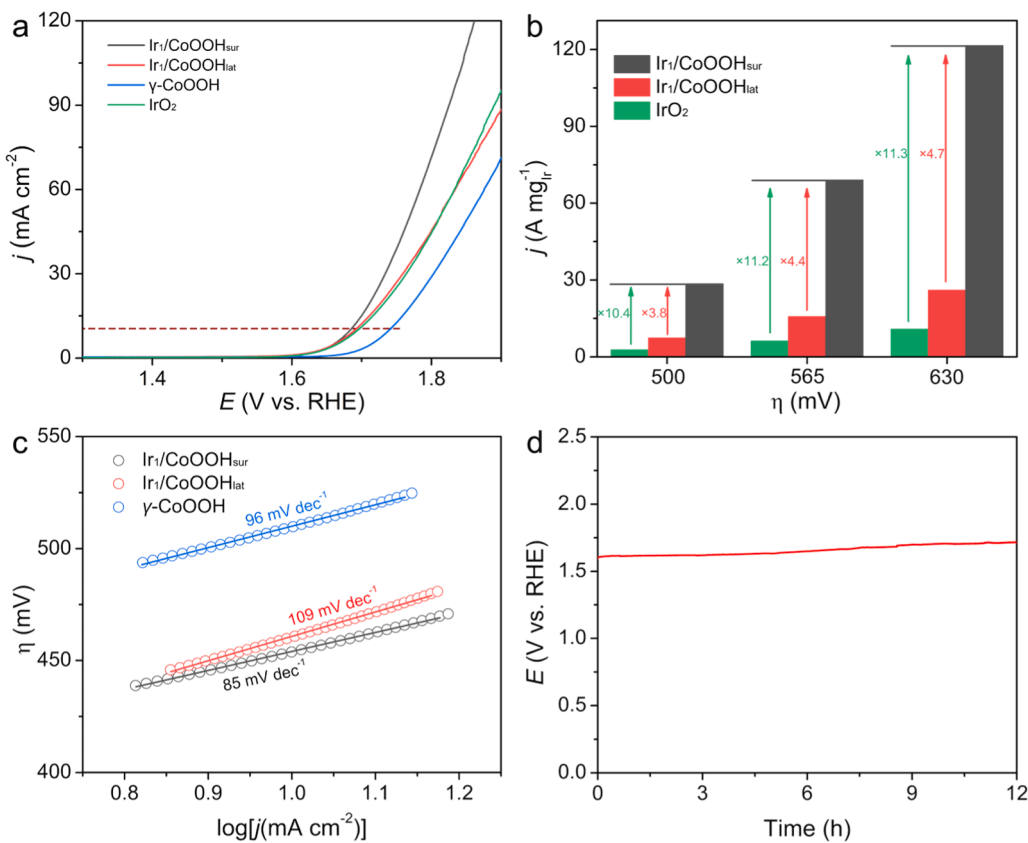


Fig. 2. Electronic and structural characterizations of  $\text{Ir}_1/\text{CoOOH}_{\text{sur}}$  and  $\text{Ir}_1/\text{CoOOH}_{\text{lat}}$ . (a) XRD patterns for  $\alpha$ - $\text{Co}(\text{OH})_2$ ,  $\gamma$ -CoOOH,  $\text{Ir}_1/\text{CoOOH}_{\text{sur}}$  and  $\text{Ir}_1/\text{CoOOH}_{\text{lat}}$ . Co 2p XPS spectra (b) and Raman spectra (c) of  $\gamma$ -CoOOH,  $\text{Ir}_1/\text{CoOOH}_{\text{sur}}$  and  $\text{Ir}_1/\text{CoOOH}_{\text{lat}}$ .



**Fig. 3.** Electrocatalytic OER performance in 1.0 M KOH. (a) Polarization curves of IrO<sub>2</sub>, γ-CoOOH, Ir<sub>1</sub>/CoOOH<sub>sur</sub> and Ir<sub>1</sub>/CoOOH<sub>lat</sub>. (b) Specific activity of IrO<sub>2</sub>, γ-CoOOH, Ir<sub>1</sub>/CoOOH<sub>sur</sub> and Ir<sub>1</sub>/CoOOH<sub>lat</sub> with the current normalized to Ir mass at different overpotentials. (c) Tafel plots for γ-CoOOH, Ir<sub>1</sub>/CoOOH<sub>sur</sub> and Ir<sub>1</sub>/CoOOH<sub>lat</sub>. (d) Chronopotentiometry curves of Ir<sub>1</sub>/CoOOH<sub>sur</sub> at a constant current density of 10 mA cm<sup>-2</sup>.

catalyst IrO<sub>2</sub>. The electrocatalytic activity of Ir<sub>1</sub>/CoOOH<sub>sur</sub> is even more notable when comparing the specific activity with the current normalized to Ir mass at different overpotentials (Fig. 3b). Specifically, the specific activity of Ir<sub>1</sub>/CoOOH<sub>sur</sub> is 5.2 times that of Ir<sub>1</sub>/CoOOH<sub>lat</sub> and 11.3 times that of IrO<sub>2</sub>, indicating that the higher OER activity originated from the discrete dangling [IrO<sub>5</sub>] motif. We calculate the ECSA of Ir<sub>1</sub>/CoOOH<sub>sur</sub> and Ir<sub>1</sub>/CoOOH<sub>lat</sub> per gram of Ir (Fig. S8). It is found that the mass-normalized ECSA of Ir<sub>1</sub>/CoOOH<sub>sur</sub> (17358 m<sup>2</sup> g<sup>-1</sup>) is far larger than that of Ir<sub>1</sub>/CoOOH<sub>lat</sub> (2676 m<sup>2</sup> g<sup>-1</sup>), which verified our initial hypothesis that coordinatively unsaturated SACs anchored atop heterogeneous catalysts are more prone to maximizing the accessibility of active sites. We also calculated the turnover frequency (TOF) based on the number of Ir atoms (Fig. S9). Ir<sub>1</sub>/CoOOH<sub>sur</sub> showed a higher TOF value than Ir<sub>1</sub>/CoOOH<sub>lat</sub> throughout the overpotential range, indicating the higher electrocatalytic performance. Moreover, both Ir<sub>1</sub>/CoOOH<sub>sur</sub> and Ir<sub>1</sub>/CoOOH<sub>lat</sub> demonstrated nearly 100% Faradaic efficiencies for OER (Fig. S10), indicating that all passed charge contributed to the exclusive evolution of O<sub>2</sub>.

We further analysed the Tafel plots and Nyquist plots to rationalize the enhanced OER performance of Ir<sub>1</sub>/CoOOH<sub>sur</sub> relative to Ir<sub>1</sub>/CoOOH<sub>lat</sub> and γ-CoOOH. The Tafel slope of Ir<sub>1</sub>/CoOOH<sub>sur</sub> (85 mV dec<sup>-1</sup>) is smaller than that of Ir<sub>1</sub>/CoOOH<sub>lat</sub> (109 mV dec<sup>-1</sup>) and γ-CoOOH (96 mV dec<sup>-1</sup>) (Fig. 3c). This suggests that Ir<sub>1</sub>/CoOOH<sub>sur</sub> demonstrated a faster OER kinetics than Ir<sub>1</sub>/CoOOH<sub>lat</sub> and γ-CoOOH. The Nyquist plots show that Ir<sub>1</sub>/CoOOH<sub>sur</sub> possessed the smallest semicircle diameter among the samples (Fig. S11), implying the minimum interfacial electron transfer resistance at the electrode-solution interface. The dramatic increase in the current density, specific activity and reaction kinetics for Ir<sub>1</sub>/CoOOH<sub>sur</sub>, in comparison with that for Ir<sub>1</sub>/CoOOH<sub>lat</sub>, γ-CoOOH and IrO<sub>2</sub>, indicates that the discrete dangling [IrO<sub>5</sub>] motif atop Ir<sub>1</sub>/CoOOH<sub>sur</sub> is the active site for OER.

The catalytic stability is essential for practical applications. In such context, the galvanostatic test was conducted to evaluate the catalytic stability of Ir<sub>1</sub>/CoOOH<sub>sur</sub> at a constant current density of 10 mA cm<sup>-2</sup>. No appreciable increment can be observed in the potential within 12 h (Fig. 3d), demonstrating the high catalytic stability. The leaching of Ir was ignorable (3.9%) after the stability test based on ICP measurements. According to the ICP result, we have further calculated the stability number (S-number) to evaluate the stability and lifetime of Ir<sub>1</sub>/CoOOH<sub>sur</sub>. The S-number significantly surpassed that of previously reported catalysts, implying its outstanding stability and lifetime (Table S4). The atomic dispersion of Ir atoms was maintained for Ir<sub>1</sub>/CoOOH<sub>sur</sub> after the durability test based on the HAADF-STEM image (Fig. S12a). The crystal and electronic structures of spent Ir<sub>1</sub>/CoOOH<sub>sur</sub> were preserved according to the Raman spectra and XPS spectra (Fig. S12b-d). SEM images and EDS spectra further manifested the catalytic stability and structural durability (Fig. S13,14).

### 3.3. Mechanistic study

We further performed density functional theory (DFT) calculations to unravel the origin of the outstanding intrinsic catalytic activity of Ir<sub>1</sub>/CoOOH<sub>sur</sub>. All the structural models were constructed on a two-layer 4 × 4 slab of γ-CoOOH (Fig. S15). The structural model of Ir<sub>1</sub>/CoOOH<sub>lat</sub> has been displayed in Fig. S16. We then calculated the projected density of states (PDOS) to visualize the influence of spatial configuration of Ir single atoms on the electronic structure of Ir<sub>1</sub>/CoOOH<sub>sur</sub> and Ir<sub>1</sub>/CoOOH<sub>lat</sub> (Fig. 4a). The PDOSs of Ir<sub>1</sub>/CoOOH<sub>sur</sub> and Ir<sub>1</sub>/CoOOH<sub>lat</sub> present a metallic behaviour due to the predominantly distributed Co, Ir, and O states across the Fermi level, therefore facilitating the interfacial electron transfer during the OER process that has been experimentally confirmed.

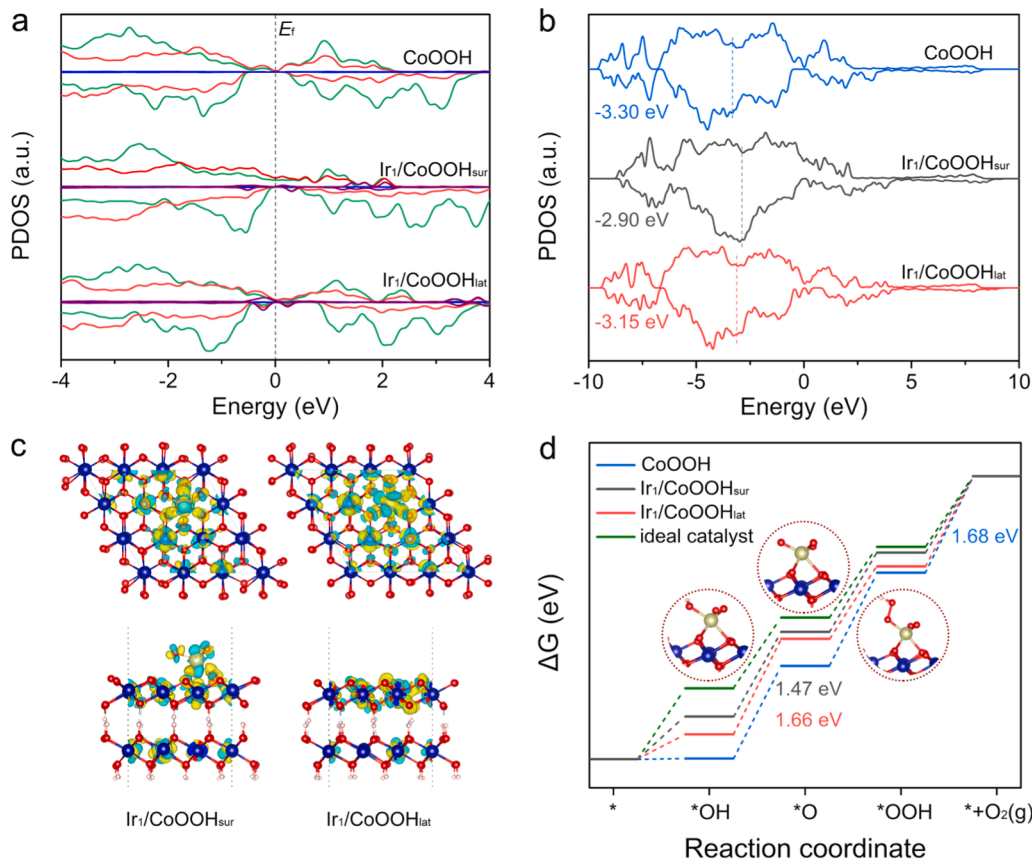


**Fig. 4.** Mechanistic study of oxygen evolution reaction using iridium single atoms with distinct spatial configuration and electronic structure. (a) PDOS and (b) O 2p-band center of  $\gamma\text{-CoOOH}$ ,  $\text{Ir}_1/\text{CoOOH}_{\text{sur}}$  and  $\text{Ir}_1/\text{CoOOH}_{\text{lat}}$ . The green, red, blue and purple line represents the PDOS of Co, O, H and Ir, respectively. (c) Differential charge density of  $\text{Ir}_1/\text{CoOOH}_{\text{sur}}$  and  $\text{Ir}_1/\text{CoOOH}_{\text{lat}}$ . (The yellow and blue contour plots represent electron accumulation and depletion, respectively). (d) Calculated free-energy diagram for OER over  $\gamma\text{-CoOOH}$ ,  $\text{Ir}_1/\text{CoOOH}_{\text{sur}}$  and  $\text{Ir}_1/\text{CoOOH}_{\text{lat}}$  relative to an ideal catalyst at  $U = 0$  V.

Altering the spatial configuration of Ir single atoms would dramatically affect the band structure and electronic distribution. The O 2p-band center is a powerful descriptor to correlate the electrocatalytic performance. Notably, the presence of Ir single atoms significantly upshifted the O 2p-band center from  $-3.30$  eV ( $\gamma\text{-CoOOH}$ ) to  $-3.15$  eV ( $\text{Ir}_1/\text{CoOOH}_{\text{lat}}$ ) and further to  $-2.90$  eV ( $\text{Ir}_1/\text{CoOOH}_{\text{sur}}$ ) (Fig. 4b). A closer O 2p-band center relative to the Fermi level generally strengthens metal-oxygen covalency, reduces adsorption energy of reaction intermediates, and endows superior OER activity [48–51]. The difference charge density analysis further reveals that electron redistribution occurred around Ir single atoms (Fig. 4c). The electron transfer from discrete dangling  $[\text{IrO}_5]$  motifs atop  $\text{Ir}_1/\text{CoOOH}_{\text{sur}}$  to adjacent oxygen is more notable, leading to more positively charged Ir compared to the  $[\text{IrO}_6]$  octahedral in  $\text{Ir}_1/\text{CoOOH}_{\text{lat}}$ . This is consistent with Bader charge analysis that Ir in  $\text{Ir}_1/\text{CoOOH}_{\text{sur}}$  possessed higher Bader charge than that in  $\text{Ir}_1/\text{CoOOH}_{\text{lat}}$  (Table S5). Previous studies demonstrated that a higher Bader charge weakens  $^*\text{OH}$  binding, which should have a direct impact on the electrocatalytic OER performance [52].

We then calculated the Gibbs free-energy diagram for OER to unravel the impacts of distinct Ir single atoms on the catalytic mechanism. The conventional adsorbate evolution mechanism (AEM) was employed for the calculation as the four concerted proton-electron transfer steps are widely considered to be the OER process for cobalt oxyhydroxides [53–55]. The observed  $^*\text{OOH}$  intermediate further confirms the validity of the conventional AEM, as evidenced by the notable peak at  $1240\text{ cm}^{-1}$  of in-situ ATR-FTIR spectra during the OER process (Fig. S17). The standard Gibbs free-energy change of OER is  $4.92$  eV and a thermodynamically ideal catalyst should require the same minimal free energy of  $1.23$  eV to form each oxygen intermediate (Fig. 4d). Interestingly, introducing Ir single atoms at varied locations of  $\gamma\text{-CoOOH}$  increased the free energies of  $^*\text{OH}$ ,  $^*\text{O}$  and  $^*\text{OOH}$  due to the weakened adsorption of oxygenated intermediates, which stems from the upshifted O 2p-band center. Moreover,  $\text{Ir}_1/\text{CoOOH}_{\text{sur}}$  displays a much weaker

adsorption capability (closer to an ideal catalyst) than  $\text{Ir}_1/\text{CoOOH}_{\text{lat}}$ , which is in line with O 2p-band center analysis and Bader charge analysis. As a result, the energy barrier of the rate-determining step (RDS) reduced from  $1.68$  eV ( $\gamma\text{-CoOOH}$ ) to  $1.47$  eV ( $\text{Ir}_1/\text{CoOOH}_{\text{sur}}$ ) and  $1.66$  eV ( $\text{Ir}_1/\text{CoOOH}_{\text{lat}}$ ). The RDS for  $\gamma\text{-CoOOH}$  is the deprotonation of  $^*\text{OOH}$ , which changed to the formation of  $^*\text{O}$  for  $\text{Ir}_1/\text{CoOOH}_{\text{sur}}$  and  $\text{Ir}_1/\text{CoOOH}_{\text{lat}}$ . Furthermore, the active center for  $\gamma\text{-CoOOH}$  and  $\text{Ir}_1/\text{CoOOH}_{\text{lat}}$  is the Co site, whereas it became the discrete dangling  $[\text{IrO}_5]$  motif for  $\text{Ir}_1/\text{CoOOH}_{\text{sur}}$  (Fig. S18–20). This should originate from the lattice configuration and electronic interaction that is associated with neighbouring Ir atoms, as Ir atoms could optimized the intermediate adsorption of adjacent Co sites and thus boosted oxygen evolution reaction [25,29]. Therefore, the spatial and electronic effects of  $\text{Ir}_1/\text{CoOOH}_{\text{sur}}$  synergistically optimized the adsorption of oxygenated intermediates and gained the lowest RDS energy barrier toward OER.

#### 3.4. Extended application in rechargeable zinc-air batteries

A rechargeable zinc-air battery (ZAB) was constructed using  $\text{Ir}_1/\text{CoOOH}_{\text{sur}}$  as the cathode catalyst to evaluable its potential application, as schematically illustrated in Fig. 5a. The open-circuit voltage of  $\text{Ir}_1/\text{CoOOH}_{\text{sur}}$ -based ZAB is drastically higher than that of  $\text{IrO}_2$ -based ZAB, indicating that the former owns better discharge capability (Fig. 5b). In addition,  $\text{Ir}_1/\text{CoOOH}_{\text{sur}}$ -based ZAB displays a higher specific capacity ( $707\text{ mAh g}_{\text{Zn}}^{-1}$ ) than  $\text{IrO}_2$ -based ZAB ( $660\text{ mAh g}_{\text{Zn}}^{-1}$ ) at a current density of  $5\text{ mA cm}^{-2}$  (Fig. 5c). A light-emitting diode (LED) light can be easily lighted by the assembled  $\text{Ir}_1/\text{CoOOH}_{\text{sur}}$ -based ZAB (Fig. 5d), which confirms its promising practical application. The maximum discharge power density ( $101\text{ mW cm}^{-2}$ ) of  $\text{Ir}_1/\text{CoOOH}_{\text{sur}}$ -based ZAB exceeds that ( $94\text{ mW cm}^{-2}$ ) of  $\text{IrO}_2$ -based ZAB (Fig. 5e). The operating stability of the ZAB is essential to its practical application. The galvanostatic charge-discharge test was hence performed to estimate the cycle stability at a current density of  $5\text{ mA cm}^{-2}$  (Fig. 5f). Remarkably, in addition to high

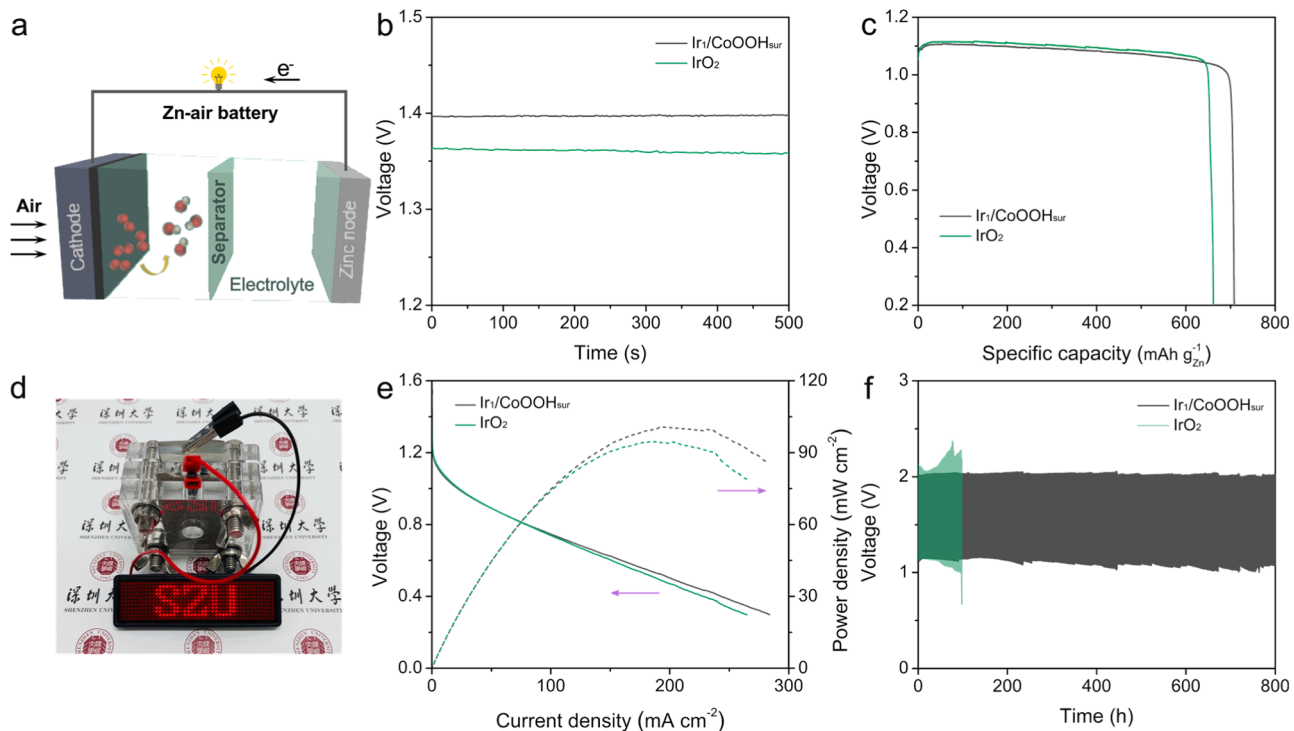
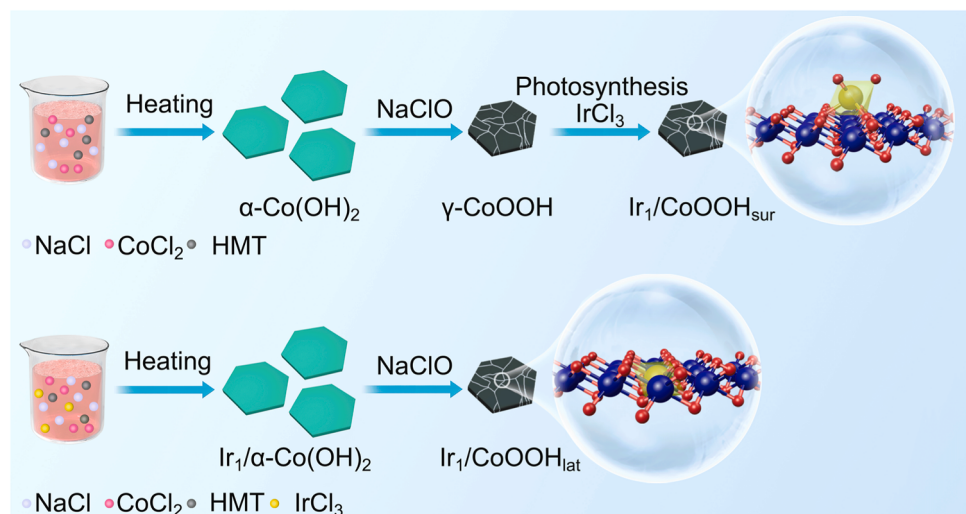


**Fig. 5.** Rechargeable ZAB performance. (a) Schematic illustration of the rechargeable ZAB. (b) Open-circuit voltage plots and (c) specific discharging capacity at a current density of  $5 \text{ mA cm}^{-2}$  with  $\text{IrO}_2$  and  $\text{Ir}_1/\text{CoOOH}_{\text{sur}}$  as the cathode catalyst. Specific capacity was normalized to consumed Zn mass. (d) Photograph of the homemade rechargeable ZAB connected to a LED light. (e) Discharging polarization and power density curves. (f) Cycling tests at a current density of  $5 \text{ mA cm}^{-2}$  (30 min for discharge followed by 30 min for charge).

battery performance,  $\text{Ir}_1/\text{CoOOH}_{\text{sur}}$ -based ZAB also shows exceptional stability and remains steady after 800 h and 1600 charge-discharge cycles, far superior to  $\text{IrO}_2$ -based ZAB. All these results demonstrate that  $\text{Ir}_1/\text{CoOOH}_{\text{sur}}$  displays higher battery performance and cycle stability than  $\text{IrO}_2$ . The battery performance of  $\text{Ir}_1/\text{CoOOH}_{\text{sur}}$  is comparable to that of the state-of-the-art catalysts (Table S6). It should be mentioned that  $\text{Ir}_1/\text{CoOOH}_{\text{sur}}$  mainly affects the ZAB performance by means of determining the OER progress rather than the oxygen reduction reaction (ORR) process. It would be interesting to investigate how  $\text{Ir}_1/\text{CoOOH}_{\text{sur}}$  behaves in the ORR process. **Scheme 1**.

#### 4. Conclusions

In summary, this work fabricated two distinct noble metal-based catalytic interfaces via altering the spatial configuration of Ir single atoms, which effectively modified the adsorption of oxygenated intermediates. The presence of Ir single atoms in both  $\text{Ir}_1/\text{CoOOH}_{\text{sur}}$  and  $\text{Ir}_1/\text{CoOOH}_{\text{lat}}$  upshifted the O *p*-band center and integrally increased the free energies of  ${}^{\bullet}\text{OH}$ ,  ${}^{\bullet}\text{O}$  and  ${}^{\bullet}\text{OOH}$ . Moreover,  $\text{Ir}_1/\text{CoOOH}_{\text{sur}}$  exerted much weaker adsorption toward all oxygenated intermediates than  $\text{Ir}_1/\text{CoOOH}_{\text{lat}}$ , rendering it the minimum RDS energy barrier toward OER. Electrochemical tests demonstrate that the electrocatalytic OER performance of  $\text{Ir}_1/\text{CoOOH}_{\text{sur}}$  outperformed that of  $\text{Ir}_1/\text{CoOOH}_{\text{lat}}$  and



**Scheme 1.** Schematic illustration of the synthesis of  $\text{Ir}_1/\text{CoOOH}_{\text{sur}}$  and  $\text{Ir}_1/\text{CoOOH}_{\text{lat}}$  via a hydrothermal method and in-situ cryogenic-photochemical strategy.

$\gamma$ -CoOOH. When serving as the cathode catalyst,  $\text{Ir}_1/\text{CoOOH}_{\text{sur}}$  exhibited higher power density (101 mW cm<sup>-2</sup>) and cycling durability (800 h) than  $\text{IrO}_2$  (94 mW cm<sup>-2</sup>, 50 h). This work showcases the possibility to push inherent spatial limits of noble metals to develop innovative electrocatalysts based on cost-effective substrates for various catalytic applications.

### CRediT authorship contribution statement

**Bo Yang:** Validation, Methodology, Data interpretation, Funding acquisition, Formal analysis, Writing - review & editing. **Meiqian Li:** Validation, Methodology, Data interpretation, Writing - review & editing. **Zhirong Zhang:** Data interpretation. **Shaoqing Chen:** Data interpretation, Formal analysis. **Miaomiao Wang:** Data interpretation. **Li Sheng:** Data interpretation, Software. **Libo Deng:** Data interpretation. **Rui Si:** Data interpretation, Formal analysis. **Maohong Fan:** Data interpretation, Formal analysis. **Huihuang Chen:** Conceptualization, Methodology, Data interpretation, Funding acquisition, Writing - original draft & editing, Project administration.

### Declaration of Competing Interest

The authors declare that they have no known competing financial interests or personal relationships that could have appeared to influence the work reported in this paper.

### Data Availability

Data will be made available on request.

### Acknowledgments

This work was financially supported by the National Natural Science Foundation of China (22005288 and 22176131), the Shenzhen Science and Technology Program (JCYJ20220818095601002 and JCYJ20210324095205015), and Department of Science and Technology of Guangdong Province (2017ZT07Z479).

### Supporting Information

DFT calculations, and corresponding additional data including TEM, SAED, AFM, BET, EXAFS, EIS, ECSA, TOF, EDS, SEM, Raman spectra, XPS, in-situ ATR-FTIR, DFT models, and adsorption configurations.

### Author contributions

All authors discussed the results and contributed to the manuscript.

### Appendix A. Supporting information

Supplementary data associated with this article can be found in the online version at [doi:10.1016/j.apcatb.2023.123227](https://doi.org/10.1016/j.apcatb.2023.123227).

### References

- B. Zhang, X. Zheng, O. Voznyy, R. Comin, M. Bajdich, M. García-Melchor, L. Han, J. Xu, M. Liu, L. Zheng, F.P. García de Arquer, C.T. Dinh, F. Fan, M. Yuan, E. Yassitepe, N. Chen, T. Regier, P. Liu, Y. Li, P. De Luna, A. Jammohamed, H.L. Xin, H. Yang, A. Vojvodic, E.H. Sargent, Homogeneously dispersed multimetal oxygen-evolving catalysts, *Science* 352 (2016) 333–337.
- L.C. Seitz, C.F. Dickens, K. Nishio, Y. Hikita, J. Montoya, A. Doyle, C. Kirk, A. Vojvodic, H.Y. Hwang, J.K. Norskov, T.F. Jaramillo, A highly active and stable  $\text{IrO}_x/\text{SrIrO}_3$  catalyst for the oxygen evolution reaction, *Science* 353 (2016) 1011–1014.
- X. Liu, Y. Yuan, J. Liu, B. Liu, X. Chen, J. Ding, X. Han, Y. Deng, C. Zhong, W. Hu, Utilizing solar energy to improve the oxygen evolution reaction kinetics in zinc-air battery, *Nat. Commun.* 10 (2019) 4767.
- B. Zhang, L. Wang, Z. Cao, S.M. Kozlov, F.P. García de Arquer, C.T. Dinh, J. Li, Z. Wang, X. Zheng, L. Zhang, Y. Wen, O. Voznyy, R. Comin, P. De Luna, T. Regier, W. Bi, E.E. Alp, C.-W. Pao, L. Zheng, Y. Hu, Y. Ji, Y. Li, Y. Zhang, L. Cavallo, H. Peng, E.H. Sargent, High-valence metals improve oxygen evolution reaction performance by modulating 3d metal oxidation cycle energetics, *Nat. Catal.* 3 (2020) 985–992.
- J. Hou, B. Zhang, Z. Li, S. Cao, Y. Sun, Y. Wu, Z. Gao, L. Sun, Vertically aligned oxygenated- $\text{CoS}_2$ – $\text{MoS}_2$  heteronanosheet architecture from polyoxometalate for efficient and stable overall water splitting, *ACS Catal.* 8 (2018) 4612–4621.
- C. Lin, J.-L. Li, X. Li, S. Yang, W. Luo, Y. Zhang, S.-H. Kim, D.-H. Kim, S.S. Shinde, Y.-F. Li, Z.-P. Liu, Z. Jiang, J.-H. Lee, In-situ reconstructed Ru atom array on  $\alpha\text{-MnO}_2$  with enhanced performance for acidic water oxidation, *Nat. Catal.* 4 (2021) 1012–1023.
- C. Wang, P. Zhai, M. Xia, Y. Wu, B. Zhang, Z. Li, L. Ran, J. Gao, X. Zhang, Z. Fan, L. Sun, J. Hou, Engineering lattice oxygen activation of iridium clusters stabilized on amorphous bimetal borides array for oxygen evolution reaction, *Angew. Chem. Int. Ed.* 60 (2021) 27126–27134.
- C. Wang, P. Zhai, M. Xia, W. Liu, J. Gao, L. Sun, J. Hou, Identification of the origin for reconstructed active sites on oxyhydroxide for oxygen evolution reaction, *Adv. Mater.* 35 (2023), 2209307.
- P. Zhai, M. Xia, Y. Wu, G. Zhang, J. Gao, B. Zhang, S. Cao, Y. Zhang, Z. Li, Z. Fan, C. Wang, X. Zhang, J.T. Miller, L. Sun, J. Hou, Engineering single-atomic ruthenium catalytic sites on defective nickel-iron layered double hydroxide for overall water splitting, *Nat. Commun.* 12 (2021) 4587.
- P. Zhai, C. Wang, Y. Zhao, Y. Zhang, J. Gao, L. Sun, J. Hou, Regulating electronic states of nitride/hydroxide to accelerate kinetics for oxygen evolution at large current density, *Nat. Commun.* 14 (2023) 1873.
- P. Zhai, Y. Zhang, Y. Wu, J. Gao, B. Zhang, S. Cao, Y. Zhang, Z. Li, L. Sun, J. Hou, Engineering active sites on hierarchical transition bimetal oxides/sulfides heterostructure array enabling robust overall water splitting, *Nat. Commun.* 11 (2020) 5462.
- H. Shi, H. Wang, Y. Zhou, J. Li, P. Zhai, X. Li, G.G. Gurzadyan, J. Hou, H. Yang, X. Guo, Atomically dispersed indium-copper dual-metal active sites promoting C-C coupling for  $\text{CO}_2$  photoreduction to ethanol, *Angew. Chem. Int. Ed.* 61 (2022), e202208904.
- W.E. Kaden, T. Wu, W.A. Kunkel, S.L. Anderson, Electronic structure controls reactivity of size-selected Pd clusters adsorbed on  $\text{TiO}_2$  surfaces, *Science* 326 (2009) 826–829.
- J. Gu, M. Jian, L. Huang, Z. Sun, A. Li, Y. Pan, J. Yang, W. Wen, W. Zhou, Y. Lin, H.-J. Wang, X. Liu, L. Wang, X. Shi, X. Huang, L. Cao, S. Chen, X. Zheng, H. Pan, J. Zhu, S. Wei, W.-X. Li, J. Lu, Synergizing metal–support interactions and spatial confinement boosts dynamics of atomic nickel for hydrogenations, *Nat. Nanotechnol.* 16 (2021) 1141–1149.
- H. Chen, X. Guo, X. Kong, Y. Xing, Y. Liu, B. Yu, Q.-X. Li, Z. Geng, R. Si, J. Zeng, Tuning the coordination number of Fe single atoms for the efficient reduction of  $\text{CO}_2$ , *Green. Chem.* 22 (2020) 7529–7536.
- H. Chen, C. Zhang, L. Sheng, M. Wang, W. Fu, S. Gao, Z. Zhang, S. Chen, R. Si, L. Wang, B. Yang, Copper single-atom catalyst as a high-performance electrocatalyst for nitrate–ammonium conversion, *J. Hazard. Mater.* 434 (2022), 128892.
- Z. Geng, Y. Liu, X. Kong, P. Li, K. Li, Z. Liu, J. Du, M. Shu, R. Si, J. Zeng, Achieving a record-high yield rate of 120.9  $\mu\text{gNH}_3 \text{ mg}_{\text{cat}}^{-1} \text{ h}^{-1}$  for  $\text{N}_2$  electrochemical reduction over Ru single-atom catalysts, *Adv. Mater.* 30 (2018), 1803498.
- J. Jones, H. Xiong, A.T. DeLaRiva, E.J. Peterson, H. Pham, S.R. Challa, G. Qi, S. Oh, M.H. Wiebenga, X.I.P. Hernández, Y. Wang, A.K. Datye, Thermally stable single-atom platinum-on-ceria catalysts via atom trapping, *Science* 353 (2016) 150–154.
- J. Liu, F.R. Lucci, M. Yang, S. Lee, M.D. Marcinkowski, A.J. Therrien, C. T. Williams, E.C.H. Sykes, M. Flytzani-Stephanopoulos, Tackling CO poisoning with single-atom alloy catalysts, *J. Am. Chem. Soc.* 138 (2016) 6396–6399.
- B. Qiao, A. Wang, X. Yang, L.F. Allard, Z. Jiang, Y. Cui, J. Liu, J. Li, T. Zhang, Single-atom catalysis of CO oxidation using  $\text{Pt}_1/\text{FeO}_x$ , *Nat. Chem.* 3 (2011) 634–641.
- B. Yang, H. Li, Z. Zhang, K. Xiao, M. Yang, F. Zhang, M. Wang, X. Guo, Q. Li, W. Fu, R. Si, L. Wang, H. Chen, Nickel dual-atom catalysts for the selective electrocatalytic de bromination of tribromoacetic acid as a green chemistry process, *Chem. Eng. J.* 427 (2022), 131719.
- Z.-Y. Wu, M. Karamad, X. Yong, Q. Huang, D.A. Cullen, P. Zhu, C. Xia, Q. Xiao, M. Shakouri, F.-Y. Chen, J.Y. Kim, Y. Xia, K. Heck, Y. Hu, M.S. Wong, Q. Li, I. Gates, S. Siahrostami, H. Wang, Electrochemical ammonia synthesis via nitrate reduction on Fe single atom catalyst, *Nat. Commun.* 12 (2021) 2870.
- C. Wan, X. Duan, Y. Huang, Molecular design of single-atom catalysts for oxygen reduction reaction, *Adv. Energy Mater.* 10 (2020), 1903815.
- Y. Xing, J. Ku, W. Fu, L. Wang, H. Chen, Inductive effect between atomically dispersed iridium and transition-metal hydroxide nanosheets enables highly efficient oxygen evolution reaction, *Chem. Eng. J.* 395 (2020), 125149.
- C. Feng, Z. Zhang, D. Wang, Y. Kong, J. Wei, R. Wang, P. Ma, H. Li, Z. Geng, M. Zuo, J. Bao, S. Zhou, J. Zeng, Tuning the electronic and steric interaction at the atomic interface for enhanced oxygen evolution, *J. Am. Chem. Soc.* 144 (2022) 9271–9279.
- Y. Yao, S. Hu, W. Chen, Z.-Q. Huang, W. Wei, T. Yao, R. Liu, K. Zang, X. Wang, G. Wu, W. Yuan, T. Yuan, B. Zhu, W. Liu, Z. Li, D. He, Z. Xue, Y. Wang, X. Zheng, J. Dong, C.-R. Chang, Y. Chen, X. Hong, J. Luo, S. Wei, W.-X. Li, P. Strasser, Y. Wu, Y. Li, Engineering the electronic structure of single atom Ru sites via compressive strain boosts acidic water oxidation electrocatalysis, *Nat. Catal.* 2 (2019) 304–313.
- J. Shan, C. Ye, S. Chen, T. Sun, Y. Jiao, L. Liu, C. Zhu, L. Song, Y. Han, M. Jaroeniec, Y. Zhu, Y. Zheng, S.-Z. Qiao, Short-range ordered iridium single atoms integrated into cobalt oxide spinel structure for highly efficient electrocatalytic water oxidation, *J. Am. Chem. Soc.* 143 (2021) 5201–5211.

[28] Q. Wang, Z. Zhang, C. Cai, M. Wang, Z.L. Zhao, M. Li, X. Huang, S. Han, H. Zhou, Z. Feng, L. Li, J. Li, H. Xu, J.S. Francisco, M. Gu, Single iridium atom doped Ni<sub>2</sub>P Catalyst for optimal oxygen evolution, *J. Am. Chem. Soc.* 143 (2021) 13605–13615.

[29] H. Chen, S. Chen, Z. Zhang, L. Sheng, J. Zhao, W. Fu, S. Xi, R. Si, L. Wang, M. Fan, B. Yang, Single-atom-induced adsorption optimization of adjacent sites boosted oxygen evolution reaction, *ACS Catal.* 12 (2022) 13482–13491.

[30] T. Zheng, C. Liu, C. Guo, M. Zhang, X. Li, Q. Jiang, W. Xue, H. Li, A. Li, C.-W. Pao, J. Xiao, C. Xia, J. Zeng, Copper-catalysed exclusive CO<sub>2</sub> to pure formic acid conversion via single-atom alloying, *Nat. Nanotechnol.* 16 (2021) 1386–1393.

[31] J. Jiao, R. Lin, S. Liu, W.-C. Cheong, C. Zhang, Z. Chen, Y. Pan, J. Tang, K. Wu, S.-F. Hung, H.M. Chen, L. Zheng, Q. Lu, X. Yang, B. Xu, H. Xiao, J. Li, D. Wang, Q. Peng, C. Chen, Y. Li, Copper atom-pair catalyst anchored on alloy nanowires for selective and efficient electrochemical reduction of CO<sub>2</sub>, *Nat. Chem.* 11 (2019) 222–228.

[32] M.D. Marcinkowski, M.T. Darby, J. Liu, J.M. Wimble, F.R. Lucci, S. Lee, A. Michaelides, M. Flytzani-Stephanopoulos, M. Stamatakis, E.C.H. Sykes, Pt/Cu single-atom alloys as coke-resistant catalysts for efficient C–H activation, *Nat. Chem.* 10 (2018) 325–332.

[33] R.T. Hannagan, G. Giannakakis, M. Flytzani-Stephanopoulos, E.C.H. Sykes, Single-atom alloy catalysis, *Chem. Rev.* 120 (2020) 12044–12088.

[34] Y. Zhang, J. Li, J. Cai, L. Yang, T. Zhang, J. Lin, X. Wang, C. Chen, L. Zheng, C.-t Au, B. Yang, L. Jiang, Construction of spatial effect from atomically dispersed Co anchoring on subnanometer Ru cluster for enhanced N<sub>2</sub>-to-NH<sub>3</sub> Conversion, *ACS Catal.* 11 (2021) 4430–4440.

[35] H. Chen, H. Li, S. Chen, L. Sheng, Z. Zhang, W. Wu, M. Fan, L. Wang, B. Yang, Atomic Pd dispersion in triangular Cu nanosheets with dominant (111) plane as a tandem catalyst for highly efficient and selective electrodehalogenation, *Appl. Catal. B: Environ.* 328 (2023), 122480.

[36] C. Tang, L. Chen, H. Li, L. Li, Y. Jiao, Y. Zheng, H. Xu, K. Davey, S.-Z. Qiao, Tailoring acidic oxygen reduction selectivity on single-atom catalysts via modification of first and second coordination spheres, *J. Am. Chem. Soc.* 143 (2021) 7819–7827.

[37] Q. Yang, H. Liu, P. Yuan, Y. Jia, L. Zhuang, H. Zhang, X. Yan, G. Liu, Y. Zhao, J. Liu, S. Wei, L. Song, Q. Wu, B. Ge, L. Zhang, K. Wang, X. Wang, C.-R. Chang, X. Yao, Understanding the activity of Co-N<sub>4-x</sub>C<sub>x</sub> in atomic metal catalysts for oxygen reduction catalysis, *J. Am. Chem. Soc.* 144 (2022) 2171–2178.

[38] H. Shang, X. Zhou, J. Dong, A. Li, X. Zhao, Q. Liu, Y. Lin, J. Pei, Z. Li, Z. Jiang, D. Zhou, L. Zheng, Y. Wang, J. Zhou, Z. Yang, R. Cao, R. Sarangi, T. Sun, X. Yang, X. Zheng, W. Yan, Z. Zhuang, J. Li, W. Chen, D. Wang, J. Zhang, Y. Li, Engineering unsymmetrically coordinated Cu-S<sub>1</sub>N<sub>3</sub> single atom sites with enhanced oxygen reduction activity, *Nat. Commun.* 11 (2020) 3049.

[39] J. Wan, Z. Zhao, H. Shang, B. Peng, W. Chen, J. Pei, L. Zheng, J. Dong, R. Cao, R. Sarangi, Z. Jiang, D. Zhou, Z. Zhuang, J. Zhang, D. Wang, Y. Li, In situ phosphatizing of triphenylphosphine encapsulated within metal–organic frameworks to design atomic Co<sub>1</sub>–P<sub>1</sub>N<sub>3</sub> interfacial structure for promoting catalytic performance, *J. Am. Chem. Soc.* 142 (2020) 8431–8439.

[40] A. Guan, Z. Chen, Y. Quan, C. Peng, Z. Wang, T.-K. Sham, C. Yang, Y. Ji, L. Qian, X. Xu, G. Zheng, Boosting CO<sub>2</sub> electroreduction to CH<sub>4</sub> via tuning neighboring single-copper sites, *ACS Energy Lett.* 5 (2020) 1044–1053.

[41] Y. Zheng, Y. Jiao, Y. Zhu, Q. Cai, A. Vasileff, L.H. Li, Y. Han, Y. Chen, S.-Z. Qiao, Molecule-level g-C<sub>3</sub>N<sub>4</sub> coordinated transition metals as a new class of electrocatalysts for oxygen electrode reactions, *J. Am. Chem. Soc.* 139 (2017) 3336–3339.

[42] C. Wu, H. Li, Z. Xia, X. Zhang, R. Deng, S. Wang, G. Sun, NiFe layered double hydroxides with unsaturated metal sites via precoated surface strategy for oxygen evolution reaction, *ACS Catal.* 10 (2020) 11127–11135.

[43] Z. Liu, R. Ma, M. Osada, K. Takada, T. Sasaki, Selective and controlled synthesis of  $\alpha$ - and  $\beta$ -cobalt hydroxides in highly developed hexagonal platelets, *J. Am. Chem. Soc.* 127 (2005) 13869–13874.

[44] X. Zheng, J. Tang, A. Gallo, J.A. Garrido Torres, X. Yu, C.J. Athanitis, E.M. Been, P. Ercius, H. Mao, S.C. Fakra, C. Song, R.C. Davis, J.A. Reimer, J. Vinson, M. Bajdich, Y. Cui, Origin of enhanced water oxidation activity in an iridium single atom anchored on NiFe oxyhydroxide catalyst, *P. Natl. Acad. Sci. USA* 118 (2021), e2101817118.

[45] J. Huang, J. Chen, T. Yao, J. He, S. Jiang, Z. Sun, Q. Liu, W. Cheng, F. Hu, Y. Jiang, Z. Pan, S. Wei, CoOOH nanosheets with high mass activity for water oxidation, *Angew. Chem. Int. Ed.* 54 (2015) 8722–8727.

[46] S. He, Y. Huang, J. Huang, W. Liu, T. Yao, S. Jiang, F. Tang, J. Liu, F. Hu, Z. Pan, Q. Liu, Ultrathin CoOOH oxides nanosheets realizing efficient photocatalytic hydrogen evolution, *J. Phys. Chem. C* 119 (2015) 26362–26366.

[47] C. Jing, T. Yuan, L. Li, J. Li, Z. Qian, J. Zhou, Y. Wang, S. Xi, N. Zhang, H.-J. Lin, C.-T. Chen, Z. Hu, D.-W. Li, L. Zhang, J.-Q. Wang, Electrocatalyst with dynamic formation of the dual-active site from the dual pathway observed by in situ Raman spectroscopy, *ACS Catal.* 12 (2022) 10276–10284.

[48] L. Giordano, K. Akkiraju, R. Jacobs, D. Vivona, D. Morgan, Y. Shao-Horn, Electronic structure-based descriptors for oxide properties and functions, *Acc. Chem. Res.* 55 (2022) 298–308.

[49] C. Ye, H. Cheng, L. Zheng, J. Lin, Q. Xu, Y. Qiu, Z. Pan, Y. Qiu, Tailoring metal–oxygen bonds boosts oxygen reaction kinetics for high-performance zinc–air batteries, *Nano Lett.* 23 (2023) 1573–1581.

[50] J. Zaffran, M.C. Toroker, Metal–oxygen bond ionicity as an efficient descriptor for doped NiOOH photocatalytic activity, *ChemPhysChem* 17 (2016) 1630–1636.

[51] Y. Wu, Y. Zhao, P. Zhai, C. Wang, J. Gao, L. Sun, J. Hou, Triggering lattice oxygen activation of single-atomic Mo sites anchored on Ni–Fe oxyhydroxides nanoarrays for electrochemical water oxidation, *Adv. Mater.* 34 (2022), 2202523.

[52] H. Huang, D. Yu, F. Hu, S.-C. Huang, J. Song, H.-Y. Chen, L.L. Li, S. Peng, Clusters induced electron redistribution to tune oxygen reduction activity of transition metal single-atom for metal–air batteries, *Angew. Chem. Int. Ed.* 61 (2022), e202116068.

[53] I.C. Man, H.-Y. Su, F. Calle-Vallejo, H.A. Hansen, J.I. Martínez, N.G. Ingólu, J. Kitchin, T.F. Jarillo, J.K. Norskov, J. Rossmeisl, Universality in oxygen evolution electrocatalysis on oxide surfaces, *ChemCatChem* 3 (2011) 1159–1165.

[54] F. Dionigi, Z. Zeng, I. Sinev, T. Merzdorf, S. Deshpande, M.B. Lopez, S. Kunze, I. Zegkinoglou, H. Sarodnik, D. Fan, A. Bergmann, J. Drnec, J.F. d Araujo, M. Gleich, D. Teschner, J. Zhu, W.-X. Li, J. Greeley, B.R. Cuanya, P. Strasser, In-situ structure and catalytic mechanism of NiFe and CoFe layered double hydroxides during oxygen evolution, *Nat. Commun.* 11 (2020) 2522.

[55] Y. Dou, D. Yuan, L. Yu, W. Zhang, L. Zhang, K. Fan, M. Al-Mamun, P. Liu, C.-T. He, H. Zhao, Interpolation between W dopant and Co vacancy in CoOOH for enhanced oxygen evolution catalysis, *Adv. Mater.* 34 (2022), 2104667.